Journal of Magnetic Resonance **148,** 289–297 (2001)
doi:10.1006/jmre.2000.2245, available online at http://www.idealibrary.com on IDEAL®

Continuous-Wave Magnetic Resonance Imaging of Short T_2 Materials

G. R. Davies, D. J. Lurie,[1] J. M. S. Hutchison, S. J. McCallum, and I. Nicholson

Department of Bio-Medical Physics and Bio-Engineering, University of Aberdeen, Foresterhill, Aberdeen AB25 2ZD, United Kingdom

Received May 12, 2000; revised October 16, 2000

There is growing interest in the use of magnetic resonance imaging (MRI) to examine solid materials where the restricted motion of the probed spins leads to broad lines and short T_2 values, rendering many interesting systems invisible to conventional 2DFT pulsed imaging methods. In EPR T_2 seldom exceeds 0.1 μs and continuous-wave methods are adopted for spectroscopy and imaging. In this paper we demonstrate the use of continuous-wave MRI to obtain 2-dimensional images of short T_2 samples. The prototype system can image samples up to 50 mm in diameter by 60 mm long and has been used to image polymers and water penetration in porous media. Typical acquisition times range between 10 and 40 min. Resolution of 1 to 2 mm has been achieved for samples with T_2 values ranging from 38 to 750 μs. There is the possibility of producing image contrast that is determined by the material properties of the sample.

Key Words: **continuous-wave; swept-field; solid imaging; high field.**

INTRODUCTION

Magnetic resonance imaging (MRI), with its ability to determine the spatial distribution of the chemical and physical properties of a sample without intrusion, has become established as a powerful and expanding analytical tool in biological science and medicine. In biological systems the motion of the spins averages out the local variations in the magnetic properties of the sample, giving narrow magnetic resonance lines and relatively long relaxation times. Under these conditions it is possible to form an image from the Fourier transformation (FT) of the signal from the spins as they evolve during a sequence of radiofrequency (RF) and magnetic field gradient pulses.

In recent years there has been increasing interest in the use of MRI to examine solid materials, porous media, and solvent diffusion in solids. Here restricted motion leads to line broadening and rapid signal decay (short T_2). Spatial resolution is ultimately limited by the maximum gradient that can be applied. These factors prevent the use of conventional pulsed FT methods and MRI equipment to examine these samples.

There are a number of techniques, still using pulsed RF, which have been developed to overcome these problems. These fall into three main types: those that reduce the linewidth through manipulation of the sample, the gradients, or the RF pulses (*1–6*), those that use large gradients to compensate for broad lines and minimize the period between pulse application and signal acquisition (*7–13*), and those that use pure phase-encoded acquisition with modest gradient strength (*14–17*).

The three most widely used approaches are oscillating magnetic field gradient imaging (*8*), stray field imaging (STRAFI) (*9–13*), and single-point ramped imaging with T_1 enhancement (SPRITE) (*14–17*). The oscillating magnetic field gradient technique uses resonant gradient coil circuits to produce large, rapidly changing gradients. RF excitation occurs when all the gradients pass through zero and a spin echo is acquired when the readout gradient reaches its maximum, and the phase gradients are again zero. STRAFI uses the very large static magnetic field gradient which exists at the end of a superconducting magnet, together with repeated acquisitions in which the sample is moved or the magnetic field or RF frequency is adjusted, to determine the spin density of successive slices through the sample. SPRITE is a pure phase-encoded method which acquires single data samples at a fixed time after RF pulses which are repeated as the magnitude of the magnetic field gradient is incremented.

Line narrowing methods tend to lose useful information from the T_2 relaxation phenomena that broaden the lines. Most of the techniques demand high RF power and place restrictions on sample size (*13, 18*).

Electron paramagnetic resonance (EPR) spectra have large linewidths, typically greater than 1 MHz, and short T_2 values (less than 1 μs). As a result most EPR spectrometers and imaging systems use continuous-wave detection (*19*). They record the changes in the electrical characteristics of the microwave cavity or RF resonator as the magnetic field is swept, bringing the spins in the sample into resonance. Before the advent of pulsed FT NMR, this method was used for all NMR experiments and was employed for NMR spectroscopy of solids as early as 1949 (*20*). We have now adopted CW NMR to image solids with very short T_2 values. We have previously demonstrated the feasibility of CW-MRI by performing one dimensional "imaging" experiments on samples of vulcanised

[1] To whom correspondence should be addressed. Fax: +44 1224 685 645. E-mail: lurie@abdn.ac.uk.

1090-7807/01 $35.00

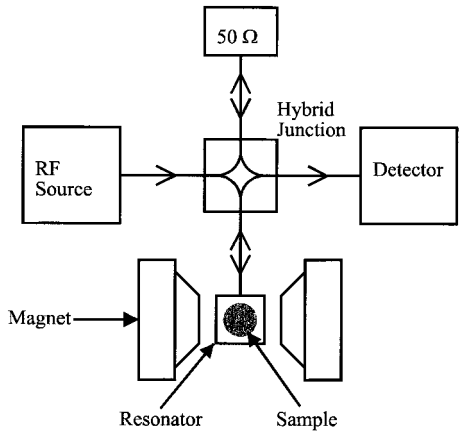

FIG. 1. Block diagram of a basic continuous-wave magnetic resonance spectrometer.

rubber, with a T_2 of ~1 ms (*21*). We have now improved and expanded the apparatus and have used it to generate 2-dimensional images of a number of short T_2 solid samples.

METHODS

CW-MR

Figure 1 shows a schematic diagram of a basic continuous-wave magnetic resonance spectrometer. The sample is placed in a resonator located in a magnetic field. A signal from a radiofrequency source is applied to one of the terminals of a hybrid junction. The resonator is tuned and matched, so that its impedance is equal to 50 Ω and the RF power is split equally between the resonator and the 50-Ω load. As the magnetic field is swept the spins reach resonance, absorbing energy and changing the impedance of the resonator. The impedance mismatch of the resonator and the load causes power to pass from the hybrid junction to the detector and a plot of detector output versus magnetic field shows the sample's magnetic resonance absorption spectrum.

The change in power as resonance is achieved is often very small compared to the electrical noise present in the circuit. Using diode detection the RF power is effectively rectified and smoothed to a DC voltage (typically about 0.5 V) with a variation as resonance is achieved of the order of 10 μV. Thus it is common practice to apply audiofrequency magnetic field modulation in addition to the sweep of the magnetic field and to use lock-in detection to select the signal with the same frequency as the modulation and at a fixed relative phase (*19*). The output from the lock-in amplifier is proportional to the change in the voltage or the power reflected from the resonator as the field is swept, i.e., it is the first derivative of the signal.

With the application of a magnetic field gradient, the spins that come into resonance are confined to a plane perpendicular to the gradient. As the main magnetic field is swept, the plane of resonance advances through the sample in the direction of the gradient. The signal from the lock-in amplifier is proportional to the change in the number of spins that are in the plane of resonance. Thus the trace over time is the first derivative of spin density of the sample projected onto the axis of the gradient. If a series of projections is acquired and the direction of the gradient rotated, in a fixed plane, between each projection, it is possible to compute the projection of spin density onto this plane. Rotating these planes can, in principle, extend reconstruction of the image to three dimensions; however, only 2-dimensional images were recorded in the work described here.

As with "conventional" MR imaging methods, the achievable spatial resolution in CW-MRI is determined by the natural linewidth, Δf, of the material being studied, and by the magnetic field gradient, G (*22*). The achievable spatial resolution can be estimated as

$$\Delta x = 2\pi\Delta f/(\gamma G), \quad [1]$$

where γ is the gyromagnetic ratio of the probed nuclei. As

$$\Delta f \cong 1/(\pi T_2), \quad [2]$$

Eq. [1] can be expressed as

$$\Delta x = 2/(\gamma G T_2). \quad [3]$$

Apparatus

Figure 2 shows a block diagram of the CW-MRI apparatus used in this work. An Oxford Instruments superconducting magnet provides a fixed 7-T field. Our homebuilt probe fits into the 183-mm bore of the magnet. The probe consists of a birdcage resonator, tuned to 300 MHz (Q = 300 when matched to 50 Ω), a split solenoid coil to provide magnetic field sweep and modulation, a Golay X-gradient coil set, and a Maxwell pair to provide the Z gradient. Figure 3 shows a schematic diagram of the probe assembly, illustrating the relative positions of the various components. The solenoid and gradient coils are wound from enameled copper wire and cooled by water. Their specification is shown in Table 1.

We have attempted to build a resonator that is as free as possible from hydrogen protons that might be picked up as a background signal. The design used is an eight-leg, high-pass birdcage resonator with diameter 52.5 mm and length 80 mm. The legs of the resonator are supported by PTFE rings (i/d 47 mm, o/d 73 mm, thickness 5 mm). The resonator, shown in Fig. 4, is capacitively coupled at the halfway points between two of the legs on the upper and lower rings to ensure that all the legs carry current and provide as uniform a B_1 field as possible. The fixed tuning capacitors are miniature chip capacitors (Tekelec, France).

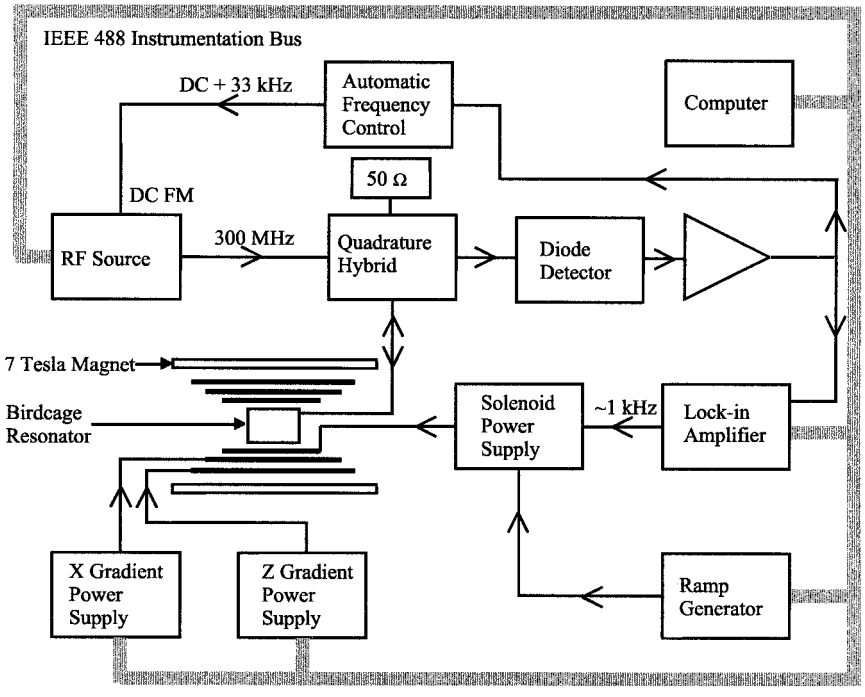

FIG. 2. Block diagram of the CW-MRI system developed in this work.

The RF shield is a brass tube with i/d 73 mm, o/d 76 mm, and length 204 mm. It is split down its length to prevent the magnetic field modulation causing eddy currents, which would cause acoustic interference and prevent the modulation from penetrating the shield to the sample. The split is closed to RF penetration by forming a capacitor comprising the shield itself, a strip of copper (width 22 mm, thickness 40 μm), which bridges the gap with a strip of PTFE (width 40 mm, thickness 25 μm) acting as the dielectric between the copper strip and the shield.

RF is supplied by a synthesiser (Hewlett Packard, Model HP8647A) to a homebuilt quadrature-hybrid junction which is connected to the resonator, a 50-Ω load, and the diode detector circuit. Figure 5 shows a schematic diagram of the quadrature-hybrid junction, which consists of a small diecast box with four BNC sockets mounted on its sides. Two $\lambda/8$ lengths of coaxial

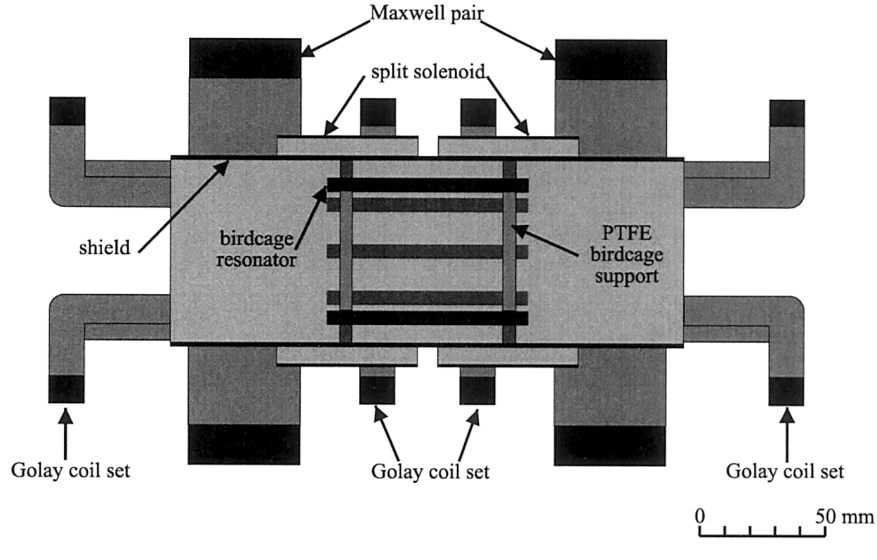

FIG. 3. Diagram of the arrangement of the resonator, shield, solenoid, and magnetic field gradient coils.

TABLE 1
Details of Magnetic Field Sweep and Modulation Coil and Magnetic Field Gradient Coils

Coil	Field sweep and modulation	*X*-gradient	*Z*-gradient
Type	Split solenoid	Golay set	Maxwell pair
Length (mm)	142	300	190
Center gap (mm)	8		101
Inner diameter (mm)	90	100	138
Outer diameter (mm)	92	122	170
No. of turns	120	28 (per segment)	144
Wire diameter (mm)	1	1.7	1.7
Resistance (Ω)	0.8	0.3	0.8
Field calibration	0.7 mT A^{-1}	9.0 mT m^{-1} A^{-1}	18.5 mT m^{-1} A^{-1}

cable connect pairs of sockets. The central conductors of the coaxial cables are coupled to each other at each end by adjustable capacitors set to about 10.6 pF (so that their impedance is equal to 50 Ω at 300 MHz).

A lock-in amplifier (Stanford Research Systems, Model 830 DSP) provides a reference signal at about 1 kHz which is fed to the solenoid power supply. Here it is added to the signal from the field sweep generator which consists of a microcomputer (Acorn, UK, Model BBC B) that produces a digital signal at the user port which is then converted to an analogue signal by a 16-bit DAC (Burr Brown DAC707).

The diode detector converts the amplitude-modulated RF signal to a signal at the modulation frequency (~1 kHz). The signal is then amplified before being split between the lock-in amplifier and an automatic frequency control (AFC). This homebuilt device (*23*) is used to ensure that any drifts in the tuning of the resonator are compensated with adjustments to the source frequency. Drifts up to ±50 kHz (equivalent to about ±1.2 mT) can be tracked with this device. Typical drifts

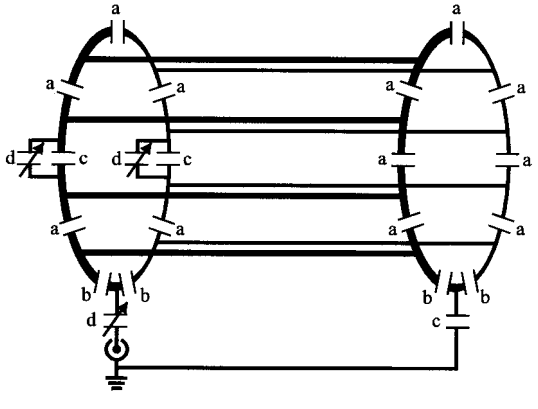

FIG. 4. The layout of the capacitors on the birdcage with the following assignments: $a \equiv 15$ pF (Tekelec, France), $b \equiv 33$ pF (Tekelec), $c \equiv 5$ pF (Tekelec), and $d \equiv 2$ to 10 pF (Oxley, UK).

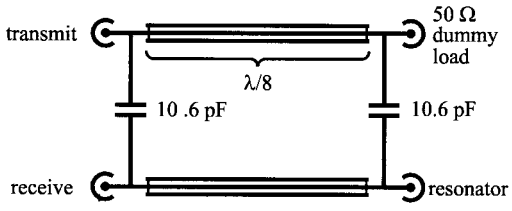

FIG. 5. Diagram of the hybrid junction.

during image collection are about 5 kHz. In some experiments we have used an output from the AFC to the solenoid power supply to match the frequency drift with a comparable magnetic field offset.

Current to generate the *X*-gradient is provided by a DC power supply (Power 10 Inc., USA, model 4680D) which drives the Golay coils. Current to generate the Z-gradient is provided by a DC power supply (Wayne Kerr, UK, Model AP6050) which drives the Maxwell pair.

The RF source, lock-in amplifier, sweep generator, and gradient supplies are controlled through an IEEE 488 GPIB bus by a microcomputer (Acorn, Model A5000) which collects the data from the lock-in amplifier and handles the sequence control as well as data and image processing.

Experimental Procedure

The sample is loaded into the resonator using a ^{1}H-free manipulator, consisting of a PTFE strap and block mounted on a glass rod. The resonator is tuned and the coupling adjusted with the aid of a network analyser (Anritsu, Japan, Model MS 3606 B). Fine tuning is then performed by observing the phase and amplitude of modulation of the power reflected from the resonator when a small (1-kHz deviation at 33 kHz) frequency modulation is applied to the source by the AFC.

Once the sample is in position and the resonator has been tuned and matched, a number of spectra are collected, without the application of a gradient. The amplitude and frequency of the magnetic field modulation, the RF power, the field sweep rate and width, and the time constants on the lock-in amplifier are adjusted to optimize the signal. These spectra also provide some insight into the bulk properties of the sample. The dependence of the signal strength on the RF power and the frequency of magnetic field modulation is related to the T_1 relaxation time of the sample whereas T_2 determines the relationship between the amplitude of magnetic field modulation and signal strength.

An appropriate gradient strength is then selected, based on the observed linewidth and desired resolution, and two projections, one along the *X*-axis and one along the *Z*-axis, are acquired. As the signal-to-noise ratio decreases with increasing gradient, if an image of a narrow-line component of the sample is desired a small gradient and small field modulation are

selected. The shorter the T_2 the larger will be the gradient strength and modulation amplitude that are used.

These two projections are then examined to confirm the choice of parameters and the positioning of the sample before the system is set to acquire and store a number of projections (typically between 15 and 65) with the gradient rotated by a small angle (π/number of projections) between each.

The projections are then baseline corrected, integrated, and baseline corrected again before being entered into a file which is submitted to a filtered back-projection program. The reconstruction program allows the possibility of deconvolution of the projections with the zero gradient spectrum; however, this is not always used as it demands that the spectral linewidth does not vary with position in the sample, and this is not necessarily the case.

RESULTS AND DISCUSSION

A number of solid objects with a range of T_2 values have been imaged with the CW-MRI system. These studies were performed primarily to test the CW-MRI methodology; nevertheless they also serve to highlight potentially useful applications of the technique. Signal-to-noise ratios (SNR) for the images, quoted in the figure legends, were determined from the ratio of the average intensity of the pixels in a region of interest to the standard deviation of the intensity.

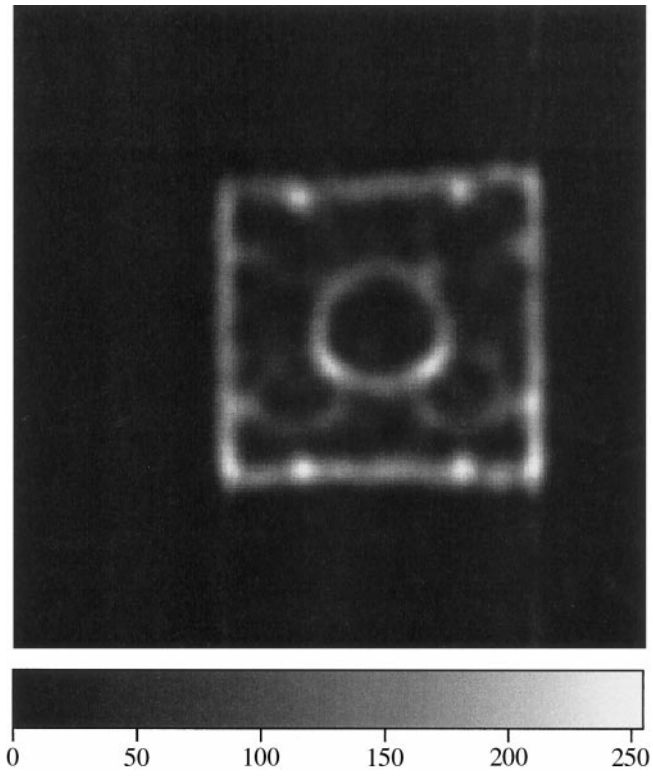

FIG. 6. CW-MRI image of Duplo ABS plastic brick (SNR = 6).

ABS Plastic Brick

An ABS plastic toy brick (Duplo) was studied. It is 30 mm in section and 19 mm in height to the "turrets," which protrude a further 5 mm from the top face. The ABS polymer in this brick has a T_2 of about 750 μs (*8*) so that it could not be imaged with a medical MRI system in standard configuration. According to Eq. [2] this T_2 gives a linewidth of 424 Hz, which is equivalent to 10 μT. We chose this item to image as its straight sides would provide an indication of the uniformity of our field gradients and other features would demonstrate the resolution of the system.

The image of the brick shown in Fig. 6 was acquired with 31 projections, each projection being the average of two 8-s sweeps, with a sweep width of 6.66 mT. The magnetic field gradient was 100 mT m^{-1}, the RF power was 10 dBm, and the field modulation amplitude was 79 μT. The total data acquisition time was approximately 10 min. The limited speed of the Acorn computer leads to image reconstruction times of the order of 5 min.

The image, a projection onto two dimensions, shows straight sides and the ribs inside the brick which are 1.5 by 1.5 mm in section can be resolved. The central support tube is evident but the turrets, which are shorter and thus contain less material, are only partially visible.

The faint streaks that project beyond the brick are an artifact of the back-projection reconstruction technique. These would be reduced if more projections were used. Such artifacts would also be less pronounced in images of an object with fewer regular features.

Perspex Phantom

A phantom made of Perspex (polymethyl methacrylate) was also studied. A diagram of the phantom is shown in Fig. 7a. Perspex has a T_2 of $\sim$38 μs (*16*), which leads to a linewidth of 8 kHz or 197 μT. The image shown in Fig. 7b was acquired with 31 projections, each taking 16 s, with a sweep width of 13.33 mT. The gradient in this case was 200 mT m^{-1}, RF power was 10 dBm, and the field modulation amplitude was 316 μT. It took 10 min to acquire the complete set of projections.

The image shows that the smallest hole, which is 2 mm in diameter, can be resolved at this gradient strength. This is in reasonable agreement with the resolution predicted from Eq. [3], which is approximately 1 mm.

Cement

The photograph in Fig. 8a shows a phantom made from calcium–aluminate cement (La Farge Aluminates, France, type Secar 80). The cement powder was mixed with water and compressed in a pot-shaped mold while setting to reduce the

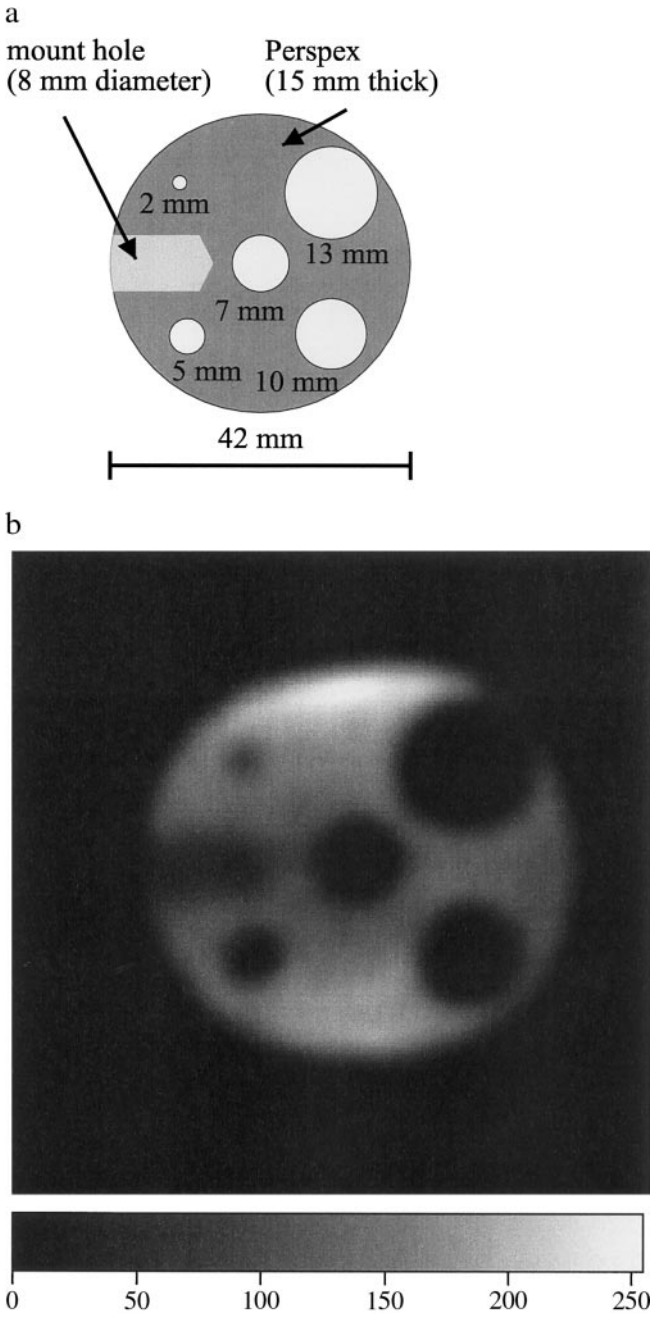

FIG. 7. (a) Diagram of the Perspex test object and (b) the corresponding CW-MRI image (SNR = 15).

pore size. The pot was not fired to remove water as would usually be the case. A ring was then sawed from the top of the pot and further cut down into three components to fit into the imager.

Figure 8b shows an image obtained with 31 projections, each projection being the average of four acquisitions taking 16 s, with a sweep width of 10.47 mT. The gradient was 150 mT m^{-1}, RF power was 10 dBm, and the field modulation amplitude was 316 μT. It took 40 min to acquire the complete set of projections. Figure 8c shows an image obtained, using the same parameters, after one of the components had been soaked in water for 40 min. The 8.3-g piece of cement was weighed before and after soaking and found to have absorbed 0.7 g of water. This shows that the technique can be used to examine water penetration of porous media. It was impossible to obtain an image of the cement sample by conventional MRI; measurements using pulsed NMR at 4.7 T indicated that the T_2^* of the water protons was approximately 65 μs.

Imbibation into Aeolian Sandstone

A cylindrical sample (length 60 mm, diameter 38 mm) of aeolian sandstone was provided by the Department of Geology and Geophysics, University of Edinburgh, UK. The end of the sample was allowed to stand in 10 mm of water for 15 s during which time it took up 1.6 g of water. Figure 9a shows the image which was obtained 30 min after imbibation. Thirty-one projections were obtained, each projection being the average of four 4-s acquisitions, with a sweep width of 10.48 mT. The gradient was 100 mT m^{-1}, RF power was 10 dBm, and the field modulation amplitude was 316 μT. Collection of the image data took approximately 13 min. Figure 9b shows an image acquired with the same parameters 5 h later. It can be seen that the distribution of the water in the sample has changed over this period. Unlike the cement, in which water chemically reacts with the cement powder, incorporating hydrogen atoms in the final product, there is no evidence of the presence of hydrogen atoms in the dry portion of the sandstone.

It should be noted that the iron content of this rock (0.32%) made it impossible to image the imbibed water by conventional MRI; measurements made on the sample using pulsed NMR at 4.7 T indicated that the T_2^* of the water protons was approximately 80 μs.

The four spots on the left and two on the right of both images are probably due to proton NMR signals from the capacitors at the end of the birdcage resonator. It is, however, curious that the same arrangement of capacitors is not visible at both ends.

Acquisition Times and Signal-to-Noise Ratios

The acquisition time in CW-MRI is largely determined by the need to extract weak signals from a noisy background using a lock-in amplifier. SNR is improved by using a long time constant for the lock-in amplifier's filter (i.e., a narrow bandwidth), which in turn requires a long field sweep time to avoid distortion of the recorded spectrum.

Although it is possible to calculate SNR theoretically, using an expression for the RF coil's thermal noise, in practice more significant contributions to noise come from radiofrequency source phase noise and noise in the preamplifier. Another source of noise that could not be eliminated was acoustic interference of the resonator from the modulation solenoid,

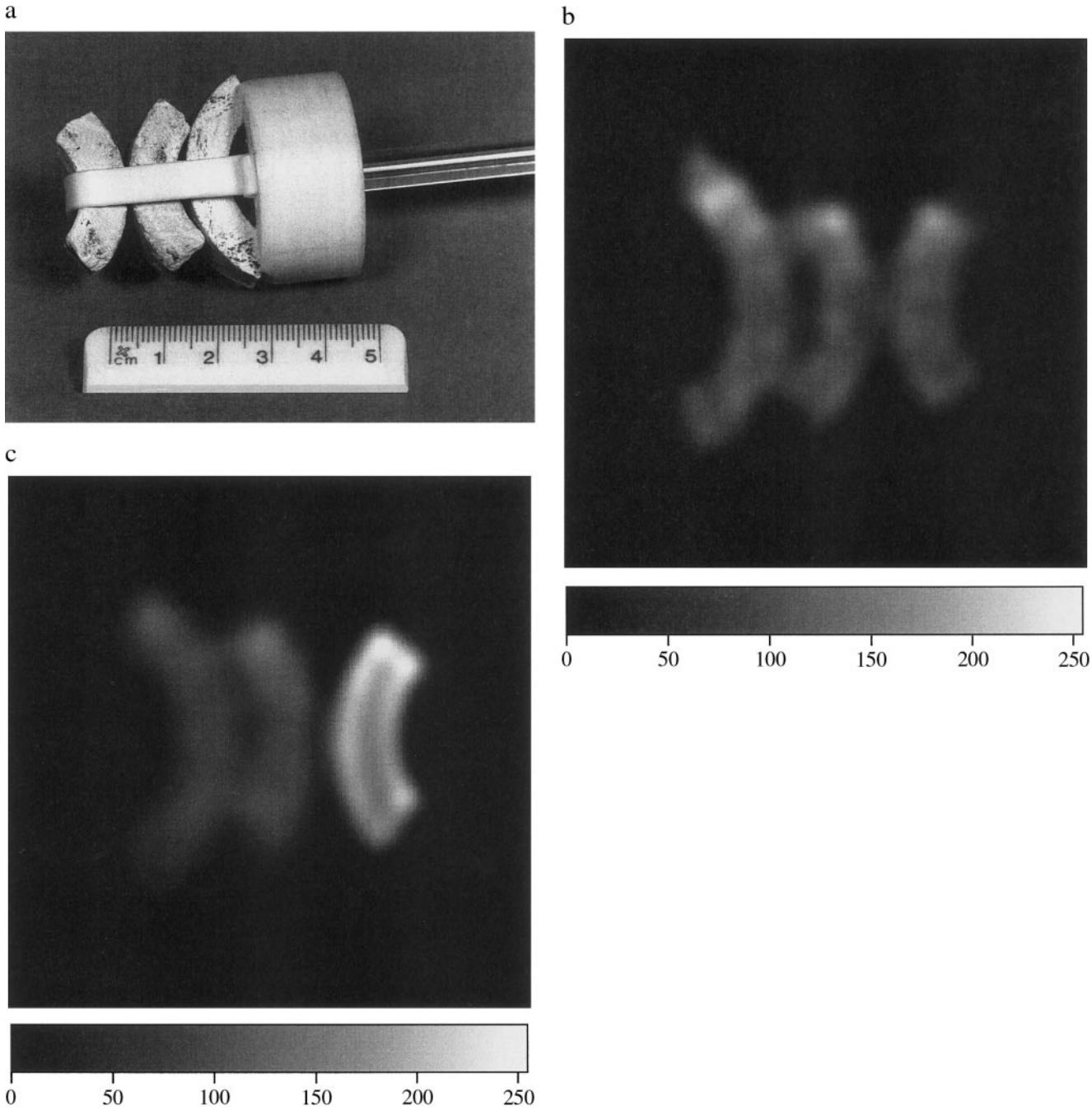

FIG. 8. (a) Calcium–aluminate test object attached to the glass rod and PTFE sample manipulator. (b) CW-MRI image from the dry cement (SNR = 10) (c) image after one of the components had been soaked in water for 5 min (SNR = 14).

occurring at the detection frequency of the lock-in amplifier. (This phenomenon is sometimes referred to as "microphonics" in CW EPR spectroscopy.) This interference probably resulted from mechanical coupling between the RF shield and the solenoid, despite attempts being made to isolate and damp the shield. It is also possible that, as the solenoid was shorter than the shield, the nonaxial component of the oscillating magnetic field was inducing eddy currents in the shield which interacted with the field from the superconducting magnet. In practice it was found that this background signal could be as much as 10 times greater than the NMR signal. Variations in its intensity, possibly caused by the changing stresses in the coil assembly, caused deviation from linearity of the projections' baselines which in turn degraded image quality. If the system was built

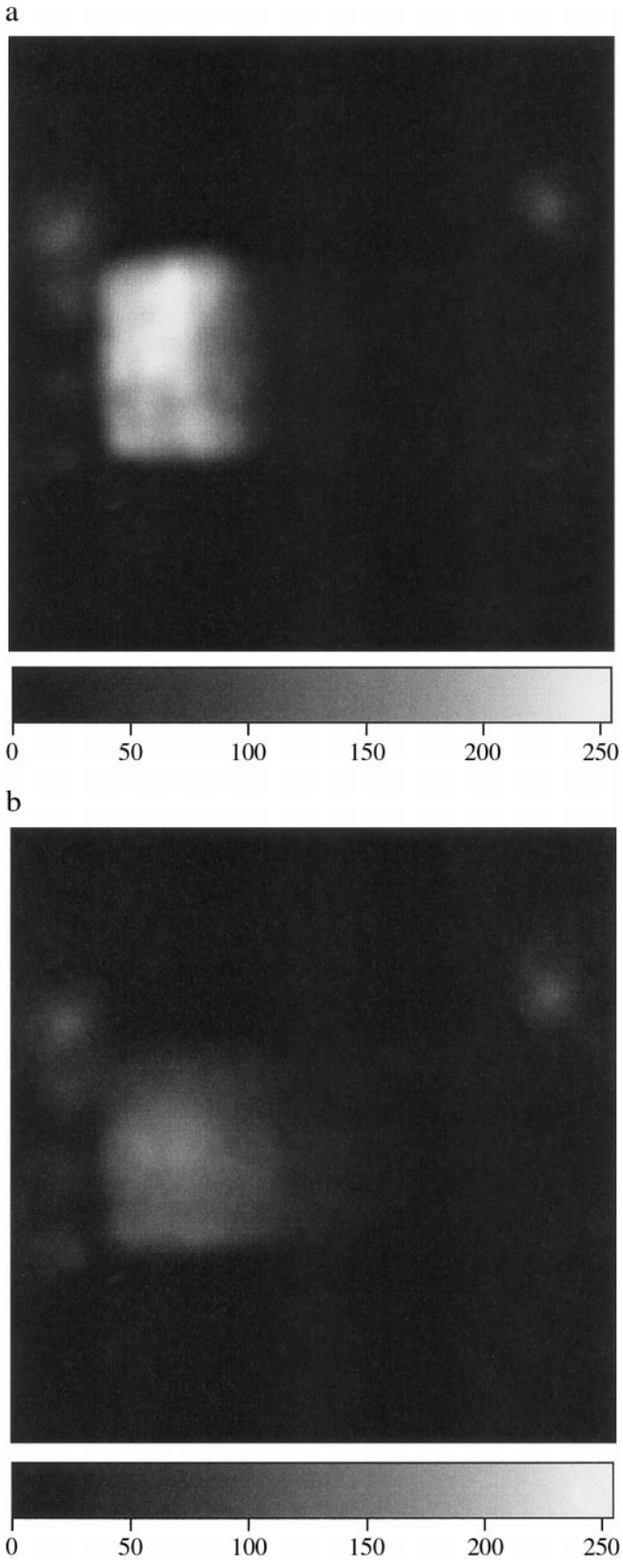

FIG. 9. CW-MRI images of water imbibed into aeolian sandstone (a) 30 min after imbibation (SNR = 12) and (b) 5 h later (SNR = 6).

again from scratch the acoustic interference could probably be reduced substantially.

CONCLUSIONS

Our prototype CW-MRI system has produced images from samples up to 45 mm in diameter and 60 mm in length, with acquisition times in the range of 10 to 40 min. Spatial resolution of about 2 mm has been realized for samples with T_2 less than 40 μs, using a gradient strength of 200 mT m^{-1}.

Pulsed solid imaging methods have the advantage that it is easy to introduce relaxation time contrast into the images, and indeed to measure the spatial variations of relaxation times in order to characterize the physical structure of the sample. Methods for quantitative mapping of relaxation parameters with CW-MRI are not nearly as straightforward; nevertheless, contrast can be introduced into the images by adjustment of the acquisition parameters, including the applied RF power and the frequency and amplitude of the magnetic field modulation. High RF power will tend to saturate spins with long T_1, reducing their signal in comparison to short T_1 samples; variation of the modulation frequency will also give T_1 contrast, since at higher modulation frequencies spins with long T_1 will be unable to "follow" the modulation and will give a smaller signal than short T_1 regions of the sample. Changing the field modulation amplitude will introduce T_2 contrast, since a broad line (short T_2) sample requires a large modulation amplitude to give its optimum signal. Using a small modulation amplitude will favor regions of the sample exhibiting a narrow linewidth. Another option is to use spectral–spatial imaging (*24*), which offers the possibility of quantifying the spatial variation of the NMR linewidth in the sample. By integrating the image over the spectral dimension a pure spin density image can be generated that is independent of linewidth and amplitude. If the relationship between the area of the spectral lines, their maximum amplitude, and their linewidth is known, the information in an intensity image and a spin density image can be used to generate a linewidth image. This technique has been used in EPR to measure the spatial variation of the linewidth of a spin probe in order to generate a tissue oxygen concentration map (*25*).

In NMR T_1 is generally much longer than in EPR, and this leads to lower RF power input before saturation occurs. Because the SNR increases with applied RF power, CW NMR is less sensitive than EPR, for the same number of spins at the same RF frequency. However, the density of hydrogen nuclei in a polymer is typically five orders of magnitude greater than that of a 1 mM concentration spin probe in a typical *in vivo* EPR experiment.

CW-MRI shows considerable potential for imaging polymers and porous media. The method has the advantage that, provided that sufficient sensitivity and gradient strength are available, it is able to study any sample, no matter how short its T_2 value, since, in contrast to pulsed magnetic resonance systems, there is no dead time or echo time during which the

signals decay. We are continuing development of the instrument to allow three-dimensional imaging, as well as imaging of other nuclei such as ^{31}P, in order to expand the range of applications of the technique.

REFERENCES

1. F. Weigand, U. Wiesner, and H. W. Spiess, Visualisation of immobilization in shear bands by NMR imaging, *Adv. Materials* **8,** 481–484 (1997).
2. S. Hafner, P. Barth, and W. Kuhn, 3D Magic-echo phase-encoded solid imaging, *J. Magn. Reson. A* **108,** 21–24 (1994).
3. S. Matsui, M. Nonaka, T. Nakai, and T. Inouye, Magic echo solid-state NMR imaging without a rapidly switchable field gradient, *J. Magn. Reson.* **138,** 220–224 (1999).
4. W. S. Veeman and G. Bijl, NMR imaging of solids with magic angle spinning, *Magn. Reson. Imaging* **10,** 755–763 (1992).
5. F. De Luca, A. Garago, B. Maraviglia, G. H. Raza, and C. Casieri, $T_{1\rho}$ space dependence in rigid polymers by effective radio frequency gradient, *Magn. Reson. Imaging* **16,** 435–440 (1998).
6. F. De Luca, S. Motta, N. Lugeri, and B. Maraviglia, Plane selection in indirect MARF Solid-State Imaging, *J. Magn. Reson. A* **121,** 114–120 (1996).
7. S. P. Cottrell, M. R. Halse, and J. H. Strange, NMR imaging of solids using large oscillating field gradients, *Meas. Sci. Technol.* **1,** 624–629 (1990).
8. S. L. Codd, M. J. D. Mallett, M. R. Halse, J. H. Strange, W. Vennart, and T. Van Doorn, A three-dimensional NMR imaging scheme utilizing doubly resonant gradient coils, *J. Magn. Reson. B* **113,** 214–221 (1996).
9. A. A. Samoilenko, D. Yu. Artemov, and L. A. Sibel'dina, Formation of sensitive layer in experiments on NMR subsurface imaging in solids, *JETP Lett.* **47,** (1988).
10. K. L. Perry, P. J. McDonald, E. W. Randall, and K. Zick, Stray field magnetic resonance imaging of the diffusion of acetone into poly-(vinyl chloride), *Polymer* **35,** 2744–2748 (1994).
11. T. Nunes, E. W. Randall, A. A. Samoilenko, P. Bodart, and G. Feio, The hardening of Portland cement studied by ^{1}H NMR stray-field imaging, *J. Phys. D Appl. Phys.* **29,** 805–808 (1996).
12. M. J. D. Mallett, M. R. Halse, and J. H. Strange, Stray field imaging by magnetic field sweep, *J. Magn. Reson.* **132,** 172–175 (1998).
13. P. J. McDonald and B. Newling, Stray field magnetic resonance imaging, *Rep. Prog. Phys.* **61,** 1441–1493 (1998).
14. B. J. Balcom, R. P. MacGregor, S. D. Beyea, D. P. Green, R. L. Armstrong, and T. W. Bremner, Single-point ramped imaging with T_1 enhancement (SPRITE), *J. Magn. Reson. A* **123,** 131–134 (1996).
15. P. J. Prado, B. J. Balcom, S. D. Beyea, R. L. Armstrong, T. W. Bremner, and P. E. Grattan-Bellew, Concrete/mortar water phase transition studied by single-point MRI methods, *Magn. Reson. Imaging* **16,** 512–523 (1998).
16. C. B. Kennedy, B. J. Balcom, and I. V. Mastikhin, Three-dimensional magnetic resonance imaging of rigid polymeric materials using single-point ramped imaging with T_1 enhancement (SPRITE), *Can. J. Chem.* **76,** 1753–1765 (1998).
17. I. V. Mastikhin, B. J. Balcom, P. J. Prado, and C. B. Kennedy, SPRITE MRI with prepared magnetization and centric *k*-space sampling, *J. Magn. Reson.* **136,** 159–168 (1999).
18. P. Jezzard, J. J. Attard, T. A. Carpenter, and L. D. Hall, Nuclear magnetic resonance imaging in the solid state, *Prog. NMR Spectrosc.* **23,** 1–41 (1991).
19. C. P. Poole, "Electron Spin Resonance," Second ed., pp. 229–233, Wiley, New York, 1983.
20. H. S. Gutowsky, G. B. Kistiakowsky, G. E. Pake, and M. E. Purcell, Structural investigations by means of nuclear magnetism. I. Rigid crystal lattices, *J. Chem. Phys.* **17,** 972–981 (1949).
21. D. J. Lurie, S. J. McCallum, J. M. S. Hutchison, and M. Alecci, Continuous-wave NMR imaging of solids, *Magn. Reson. Mat. Phys. Biol. Med. (MAG*MA)* **4,** 77–81 (1996).
22. P. T. Callaghan, "Principles of Nuclear Magnetic Resonance Microscopy," Clarendon Press, Oxford, 1991.
23. M. Alecci, S. J. McCallum, and D. J. Lurie, Design and optimisation of an automatic frequency control system for a radiofrequency electron paramagnetic resonance spectrometer, *J. Magn. Reson. A* **117,** 272–277 (1995).
24. M. M. Maltempo, S. S. Eaton, and G. R. Eaton, Spectral–spatial two-dimensional EPR imaging, *J. Magn. Reson.* **72,** 449–455 (1987).
25. S. S. Velan, R. G. S. Spencer, J. L. Zweier, and P. Kuppusamy, Electron paramagnetic resonance oxygen mapping (EPROM): Direct visualization of oxygen concentration in tissue, *Magn. Reson. Med.* **43,** 804–809 (2000).